

Reverse time imaging of ground-penetrating radar and SH-seismic data including the effects of wave loss

Tieyuan Zhu¹, José M. Carcione², and Marco A. B. Botelho³

ABSTRACT

The presence of wave loss (velocity dispersion and attenuation in lossy media) degrades the resolution of migrated images by distorting the phase and amplitude of the signal. These effects have to be mitigated to improve resolution. We have developed a technique to perform reverse time migration of ground-penetrating radar and SH-seismic data in lossy media, suitable for engineering and seismic applications. The method is based on the solution of the transverse magnetic (TM) Maxwell equation, which in view of the acoustic-electromagnetic analogy, is mathematically equivalent to the SH-wave equation, where attenuation is described by the Maxwell mechanical model. Attenuation compensation is performed by reversing the sign of the diffusion term (first-order time derivative). In this manner, the TM equation has

the same wave-velocity dependence with frequency (same velocity-dispersion behavior) but opposite attenuation, i.e., compensating for attenuation effects when back propagating. We have solved the equations numerically with a direct grid method by using the Fourier pseudospectral operator for computing the spatial derivatives, and we used an explicit staggered second-order finite-difference approximation for computing the time derivative. Four applications illustrated the potential of the algorithm. The migrated image by correcting for attenuation loss is able to improve the illumination of the target reflectors. This migration is found to be particularly useful to balance the overall image amplitude by illuminating shadow zones. Under the assumption of low-loss media (e.g., $Q \gg 1$) and thicknesses comparable with or smaller than the skin depth, the attenuation-compensated migration is stable.

INTRODUCTION

Ground-penetrating radar (GPR) has become an important shallow subsurface exploration tool (e.g., Owen, 1995; Miller et al., 2010; Slob et al., 2010). It has been used for a wide range of engineering and environmental problems, recently facilitated by the application of standard seismic techniques, such as multifold coverage and processing (e.g., Bradford, 2006). This high-frequency electromagnetic (EM) technique is conceptually similar to the seismic reflection method (Carcione and Cavallini, 1995a), and therefore, many of the algorithms used in oil exploration can be applied, with minor modification, to the interpretation of georadargrams. For example, Zhdanov and Frenkel (1983) propose a method of reverse time continuation of the EM field, which is analogous to the seismic reverse time migration (RTM) (Baysal et al., 1983; McMechan, 1983). A complete overview can be found in Zhdanov (2009).

Radar signals, as well as seismic waves, are affected by loss mechanisms. In GPR applications, the most important are ionic currents, related to the electric conductivity. It is well known from laboratory and field data that it is essential to model dissipation effects. For most rocks, EM Q is lower than seismic Q , implying stronger loss effects. Mainly, the presence of mineralized water in pores and fractures is responsible. In the seismic case, the loss effects are described by an effective Maxwell viscosity, that represented by a dashpot in the well-known Maxwell mechanical model composed of a spring and a dashpot connected in series (Carcione and Cavallini, 1995b).

Proper imaging of objects and interfaces require to account for the attenuation and dispersion effects of the underground, possibly using prestack depth migration based on a full-wave equation or using the concept of exploding reflector in the case of poststack

Manuscript received by the Editor 23 July 2015; revised manuscript received 17 January 2016; published online 30 May 2016.

¹Formerly University of Texas at Austin, Jackson School of Geosciences, Austin, Texas, USA; presently Pennsylvania State University, Department of Geosciences, Institute of Natural Gas Research, University Park, Pennsylvania, USA. E-mail: tieyuanzhu@gmail.com.

²Istituto Nazionale di Oceanografia e di Geofisica Sperimentale (OGS), Trieste, Italy. E-mail: jcarcione@inogs.it.

³Universidade Federal da Bahia, Instituto de Geociências/CPGG, Campus Universitário de Ondina, Salvador-BA, Brasil. E-mail: botelho@cpgg.ufba.br.

© 2016 Society of Exploration Geophysicists. All rights reserved.

depth migration (e.g., Baysal et al., 1983; Fischer et al., 1992; Pestana and Botelho, 1997; Di and Wang, 2004; Zhou et al., 2005; Bradford, 2015). A review of imaging methods, in the case of lossless media, is given in Özdemir et al. (2014), where the authors illustrate and compare different migration algorithms.

Over the past two decades, the seismic community has developed many migration algorithms using one-way frequency-domain equations to compensate for attenuation and dispersion effects (e.g., Dai and West, 1994; Yu et al., 2002). Recent efforts using two-way time-domain wave equations have been made. Zhang et al. (2010) propose a viscoacoustic wave equation for compensating attenuation and phase dispersion effects. Their equation is based on a constant- Q model (Kjartansson, 1979); i.e., attenuation is considered to be approximately linear with frequency. Zhu and Harris (2014) introduce a viscoacoustic wave equation without memory variables, accounting for attenuation by incorporating a fractional Laplacian operator in the space-time domain. Zhu et al. (2014) implement the technique to Q -compensated RTM. Later, it has been applied to seismic field data for delineating a hydrocarbon reservoir body in west Texas oilfield (Zhu and Harris, 2015). Alternatively, Dutta and Schuster (2014) use a linearized 2D viscoacoustic wave equation based on the Zener model, written in the particle velocity-stress formulation. Its adjoint formula is introduced by Blanch and Symes (1995). The method is adapted from conventional least-squares migration (LSM) and reconstructs the earth reflectivity image from the recorded waveform data under the Born approximation. Sun et al. (2015) precondition Q -LSM with an inverse viscoacoustic operator, which is designed for RTM by Zhu et al. (2014), so as to speed-up the migration with fast convergence.

On the other hand, there are very limited studies in the GPR community on this topic. Di and Wang (2004) present a poststack RTM approach based on the second-order homogeneous Maxwell equation to consider attenuation and dispersion, but it is not clear if attenuation effect is compensated for during migration. Similarly, Bradford (2015) develops RTM with topography and conductivity loss. With normalized crosscorrelation imaging condition, attenuation effects are compensated for forward propagation but not for backward propagation, thus incomplete compensation (for detailed explanation, see Zhu, 2016). Sena et al. (2006) solve the Q -compensation migration problem with the split-step Fourier technique in the frequency domain and introduce a homogeneous plane-wave approximation to stabilize the algorithm in the presence of attenuation. The approximation holds for waves whose attenuation direction coincides with the propagation direction, which is not the case in attenuating media because transmitted waves at an interface are inhomogeneous. Use of a suitable wave equation is not only important in RTM but also in full-waveform inversion (FWI), to build proper high-resolution images of the subsurface (Lavoué et al., 2014).

This paper presents a theory and algorithm of attenuation-compensated migration based on the TM Maxwell equation in 2D. To extrapolate radar data back in time with attenuation and dispersion compensation, the sign of the diffusion term is reversed, which results in the same velocity dispersion as the Maxwell equation but a negative Q factor. We show this property numerically in a homogeneous medium. To avoid amplifying the high-frequency noise during the extrapolation, we use a low-pass filter for the attenuation and dispersion operators in the wavenumber domain. The reverse time (or exploding reflector) imaging condition is applied for

zero-offset or poststack data and zero-lag crosscorrelation imaging for prestack data. The resulting RTM images are not affected by loss effects.

We begin by reviewing the TM equation and analogous SH-wave equation, introducing the time-reversed TM equation and their attenuation compensated formula, respectively. Then, we describe the reverse time imaging conditions for poststack and prestack migrations. Finally, we present applications of the migration algorithm.

THE MAXWELL AND SH-WAVE EQUATIONS

We compute synthetic radargrams by using the Maxwell equation. Let us assume that the propagation is in the (x, z) -plane, and that the material properties are invariant in the y -direction. Then, E_x , E_z , and H_y are decoupled from E_y , H_x , and H_z . In the absence of electric source currents, the first three field components obey the transverse magnetic (TM) field differential equations (e.g., Carcione, 1996a):

$$\begin{aligned} \frac{\partial E_z}{\partial x} - \frac{\partial E_x}{\partial z} &= \mu \frac{\partial H_y}{\partial t}, \\ -\frac{\partial H_y}{\partial z} &= s\sigma E_x + \epsilon \frac{\partial E_x}{\partial t} + J_x, \\ \frac{\partial H_y}{\partial x} &= s\sigma E_z + \epsilon \frac{\partial E_z}{\partial t} + J_z, \end{aligned} \quad (1)$$

where t is the time variable, μ is the magnetic permeability, ϵ is the dielectric permittivity, σ is the conductivity, J denotes electric sources, and $s = 1$. The introduction of the quantity s will be clear below.

Equation 1 corresponds to the SH-wave equation in seismology, so that the problem solved here also holds for seismic S-waves with loss. Carcione and Cavallini (1995a) establish the mathematical analogy between SH- and TM-waves, where the former are S-waves polarized in the horizontal plane. To apply the analogy, the equivalence is

$$\begin{aligned} H_y &\Leftrightarrow v_y, \\ E_x &\Leftrightarrow -\sigma_{yz}, \\ E_z &\Leftrightarrow \sigma_{xy}, \\ \epsilon &\Leftrightarrow G^{-1}, \\ \sigma &\Leftrightarrow \eta^{-1}, \\ \mu &\Leftrightarrow \rho, \end{aligned} \quad (2)$$

where v_i and σ_{ij} denote particle velocity and stress components, G is the shear modulus, η is the viscosity, and ρ is the density. The resulting SH-wave equation is a generalization of the elastic equation with the incorporation of the Maxwell mechanical model to describe the anelastic effects (Carcione [2014], chapter 8). However, the technique present here can also be applied to the SH-wave equation described by Zener elements (Carcione and Cavallini, 1995b). The generalization to anisotropy, in the EM and seismic cases (see equations in Carcione and Cavallini, 1995a), is also straightforward.

DISPERSION RELATION AND ATTENUATION COMPENSATION

Considering a homogeneous medium and ignoring sources, equation 1 can be written as

$$\frac{\partial^2 H_y}{\partial t^2} = \frac{1}{\epsilon\mu} \nabla^2 H_y - s \frac{\sigma}{\epsilon} \frac{\partial H_y}{\partial t}, \quad (3)$$

where the above-mentioned equation simulates TM-waves with electrical conductivity that describes EM attenuation. A similar equation 3 can be obtained using the electric-field components. The second term in the right side corresponds to the attenuation effects, which indicate the amplitude loss and the dispersion of the waves.

Substituting a Fourier plane-wave kernel into equation 3, yields the complex velocity (Carcione, 2014)

$$v = [(\epsilon - is\omega^{-1}\sigma)\mu]^{-1/2}, \quad (4)$$

where ω is the angular frequency. To implement the RTM algorithm, we have to use the Maxwell equation time-reversed. In the implementation, this procedure is completed by flipping the data in time. According to the principle of time invariance in attenuating media (Zhu, 2014), attenuation compensation can be accomplished by reversing the sign of the first-order time derivative term in equation 3. Therefore, the forward TM equation and time-reversed TM equation with attenuation compensation can be obtained from equation 1 with $s = -1$. It also states that the TM equation for reverse time propagation is time-invariant when $s = -1$.

Let us consider the dispersion relation. Taking $s = -1$ in equation 4, the complex velocity is

$$v = [(\epsilon + i\omega^{-1}\sigma)\mu]^{-1/2}. \quad (5)$$

From equations 4 and 5, the phase velocity and attenuation factors are (Carcione, 2014)

$$v_p = [\text{Re}(v^{-1})]^{-1} = \left[\frac{\mu\epsilon}{2} \left(\sqrt{1 + \left(\frac{\sigma}{\omega\epsilon}\right)^2} + 1 \right) \right]^{-1/2},$$

$$\alpha = -\omega \text{Im}(v^{-1}) = \text{sgn}\left(\frac{\mu\sigma}{\omega}\right) \omega \left[\frac{\mu\epsilon}{2} \left(\sqrt{1 + \left(\frac{\sigma}{\omega\epsilon}\right)^2} - 1 \right) \right]^{1/2}, \quad (6)$$

where $\text{sgn}(x)$ is 1 when $x > 0$ and -1 when $x < 0$, and the quality factor Q is

$$Q = \frac{\text{Re}(v^2)}{\text{Im}(v^2)} = \omega \frac{\epsilon}{\sigma}. \quad (7)$$

As can be seen, attenuation compensation ($s = -1$) leads to negative α and negative $Q = -\omega\epsilon/\sigma$, and changing the sign of the imaginary part in equation 5 only affects the attenuation Q because the phase velocity v_p remains the same. This is analogous to viscoacoustic time-reversal imaging (Zhu, 2014). To show this, we consider the following example: $\epsilon = 6 \epsilon_0$, where $\epsilon_0 = 8.85 \times 10^{-12} \text{ F m}^{-1}$, $\mu = \mu_0 = 4\pi \times 10^{-7} \text{ H m}^{-1}$, and $\sigma = 0.1 \text{ S/m}$. Figure 1 shows the phase velocity and attenuation factor for the forward and reversed

cases. The velocity is normalized with the light velocity in vacuum, $c_0 = 1/\sqrt{\mu_0\epsilon_0}$. As can be seen, the dispersion effects are the same, but the attenuation factors have opposite signs. This ensures that time-reversal modeling recovers the amplitude (Q -compensation), while preserving the phase velocity of each Fourier component.

The TM equation 1 and its inverse equation (i.e., equation 1 with $s = -1$) are the basis of the migration algorithm used to back-propagate the field vector $(H_y, E_x, E_z)^T$. Boundary (absorbing) conditions are given by the split perfectly matched layer (PML) method on all sides of the mesh, whose equations are

$$\begin{aligned} \frac{\partial E_x}{\partial t} + \epsilon^{-1}\sigma E_x + \alpha_x E_x &= -\epsilon^{-1} \frac{\partial H_y}{\partial z}, \\ \frac{\partial E_z}{\partial t} + \epsilon^{-1}\sigma E_z + \alpha_z E_z &= \epsilon^{-1} \frac{\partial H_y}{\partial x}, \\ \frac{\partial H_{y1}}{\partial t} + \alpha_x H_{y1} &= \mu^{-1} \frac{\partial E_z}{\partial x}, \\ \frac{\partial H_{y2}}{\partial t} + \alpha_z H_{y2} &= -\mu^{-1} \frac{\partial E_x}{\partial z}, \\ H_y &= H_{y1} + H_{y2}, \end{aligned} \quad (8)$$

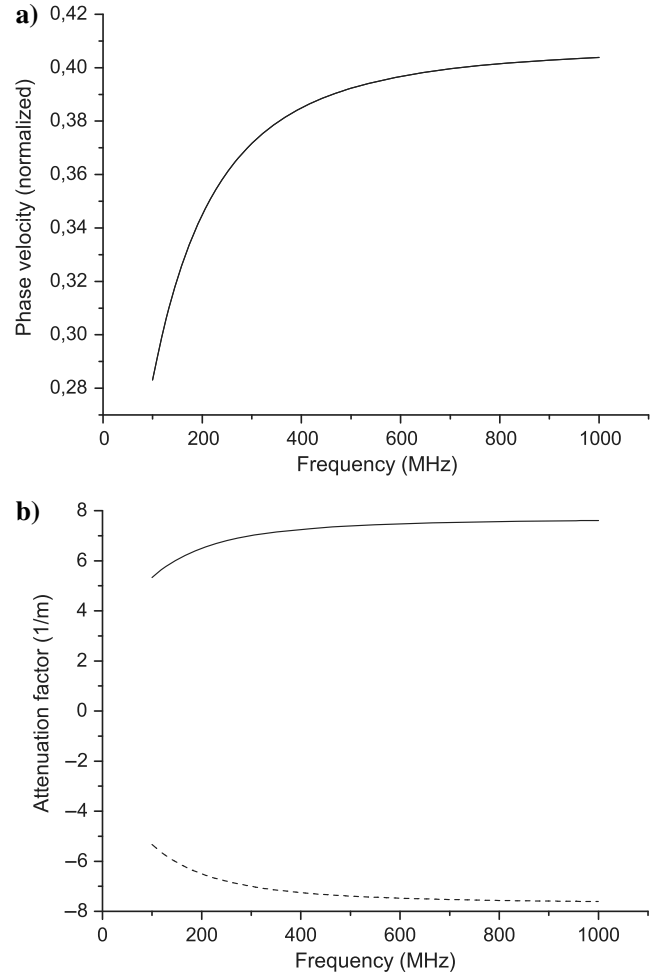


Figure 1. (a) Phase velocity and (b) attenuation factor corresponding to the forward (solid line) and time-reversed (dashed line) equations. The velocity is normalized with the light velocity in vacuum. Both wave velocities coincide.

where α_x and α_z are the damping parameters used only within the PML. Following Yuan et al. (1999) (equation 24), the split field equation 8 can be transformed into an exponential form that allows larger attenuation without numerical instability. Equation 8 is solved with a direct grid method that computes the spatial derivatives using the Fourier pseudospectral method, where the electric E_x and E_z fields are evaluated on staggered spatial grids (Carcione et al., 1999). The solution is computed with an explicit staggered second-order finite-difference approximation of the time derivative.

REVERSE TIME EXTRAPOLATION IMAGING CONDITION

Stacked or zero-offset data can be simulated with the exploding-reflector method (Claerbout, 1985) as follows: All reflectors at time $t = 0$ are treated as sources in the subsurface, where the wave equation upward propagates the energy and each receiver records a time history. On the other hand, the reverse time extrapolation (exploding-reflector imaging) is performed by propagating the recorded wave energy at the receivers back in time to the sources using half the wave velocity. Similarly, the reverse time extrapolation is implemented by solving the TM equation. Halving the wave velocity is achieved by multiplying by four the magnetic permeability μ (see equation 4), which ensures that the amplitude decay corresponds to that of the two-way travel path (Carcione et al., 2002). The recorded data at the receivers are enforced as a boundary condition, acting as sources. This extrapolation is continued backward in time to $t = 0$, when all depths are imaged simultaneously. The final

image is formulated as $I(\mathbf{x}) = H_y(\mathbf{x}, t = 0)$, where \mathbf{x} is the image location.

To compensate for attenuation losses, we solve the time-reversed TM equation (setting $s = -1$ in equation 1) similar to the extrapolation of acoustic waves in attenuating media performed by Zhu (2014). Similarly, the full RTM imaging condition can be applied to multiple offset or prestack GPR data. Briefly, this kind of RTM algorithm, analogous to viscoacoustic RTM, consists of three steps (Zhu et al., 2014):

- 1) Forward propagation with equation 1 ($s = +1$), obtaining the source wavefield $S(\mathbf{x}, t)$ in the model space, where \mathbf{x} is the position vector (propagation from source to scatter).
- 2) Back propagation of the measured data with equation 1 ($s = -1$), obtaining the receiver wavefield $R(\mathbf{x}, t)$, i.e., use the data as a boundary condition and propagate it back in time from the receiver to the scatterer.
- 3) Application of an imaging condition, e.g., a zero-lag crosscorrelation condition

$$I(\mathbf{x}) = \int_0^T S(\mathbf{x}, t)R(\mathbf{x}, t)dt, \quad (9)$$

where T is the maximum recording time of the data. Deconvolution/source-normalized crosscorrelation imaging condition can also be used for approximating the reflectivity (Zhu, 2015).

When compensating for attenuation, a problem is the amplification of high-frequency noise present in the data. To prevent this, we use a low-pass filter in the wavenumber domain. The cutoff wavenumber is calculated from the cutoff frequency based on the maximum phase velocity of the model. Zhu (2015) shows that using a Tukey low-pass filter, the cutoff frequency is more influential on the image resolution than the taper ratio. We estimated the suitable cutoff frequency by identifying the noise in the spectrum of the observed data.

From the previous analysis (Zhu et al., 2014), the loss compensation using the EM equation 1 is able to recover the amplitude loss as in the non-attenuating case; i.e., the final image will not be affected by the attenuation if the related properties are well defined, e.g., by attenuation tomography (e.g., Liu et al., 1998; Hinz and Bradford, 2010) or FWI (e.g., Busch et al., 2012; Lavoué et al., 2014).

GPR EXAMPLES

Homogeneous media

We first consider a homogeneous medium to show the attenuation effects using the TM equation 1. Forward propagation is performed with $s = 1$. The physical properties and modeling parameters are $\epsilon = 10 \epsilon_0$, $\mu = \mu_0$, the time step is 0.05 ns, the grid spacing is 0.02 m, and the mesh is square with 512 points per side. A Ricker

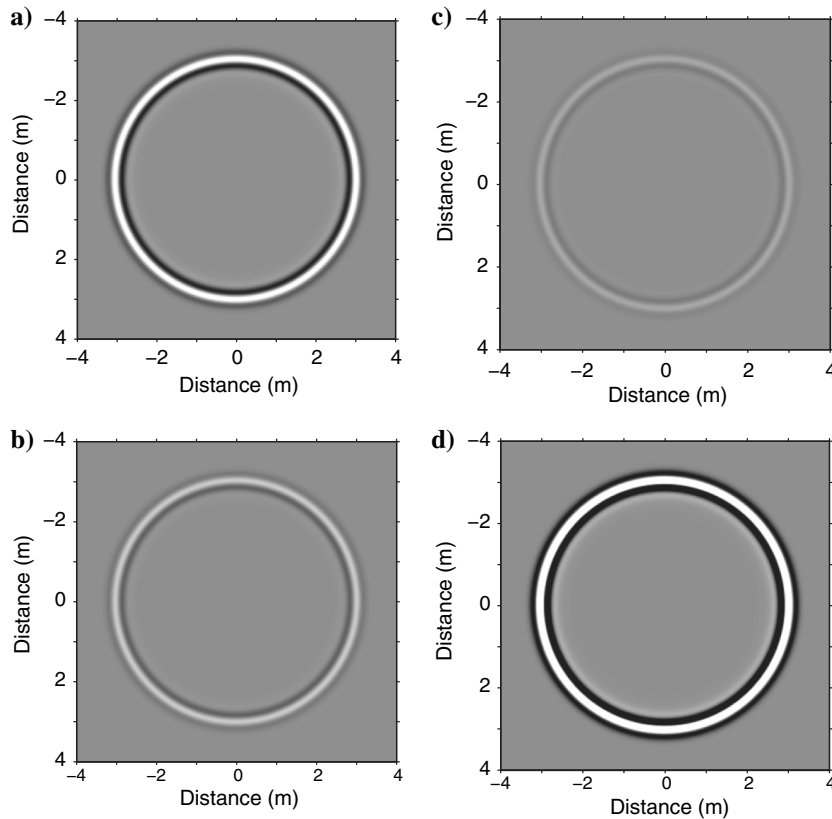


Figure 2. Snapshots of the H_y wavefield at 25 ns, corresponding to (a) $\sigma = 0$ (lossless), (b) $\sigma = 0.005$, (c) $\sigma = 0.01$, and (d) $\sigma = 0.005$ S/m, but $s = -1$.

wavelet with a central frequency of 300 MHz is used as a source. Figure 2a–2c shows three snapshots of the H_y component at 38 ns with $\sigma = 0, 0.005,$ and 0.01 S/m, respectively. As can be seen, there is increasing attenuation with increasing electrical conductivity. Then, we perform a simulation with $s = -1$. Figure 2d shows a snapshot of the H_y component at 25 ns with $\sigma = 0.005$ S/m. The amplitude is thus amplified compared with Figure 2a.

Let us consider low-loss media, for which $Q \gg 1$, i.e., $\sigma \ll \epsilon\omega$. In this limit, the skin depth is $d = \sqrt{2/\omega\sigma\mu}$. For instance, when $\sigma = 0.01$ S/m, Q is 11 and the skin depth is 1.68 m. Figure 3 shows the waveform at five different offsets (0.1, 1, 2, 3, and 4 m). The waveform is normalized by the peak amplitude at 0.1 m offset. Note that the peak amplitude at 2 m offset is approximately 0.1 of the reference one (at 0.1 m). We infer that it is possible to recover the amplitude when the wave propagates through a layer, whose thickness is comparable or smaller than the skin depth.

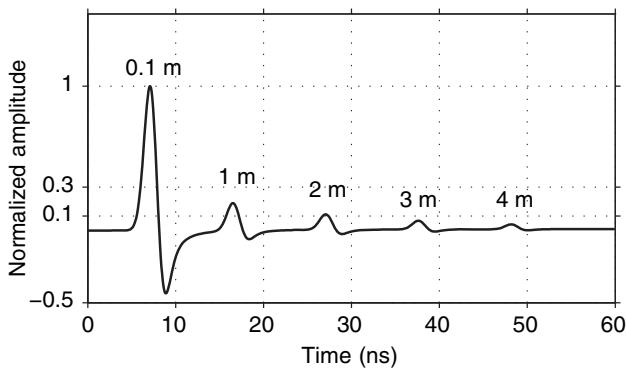


Figure 3. Waveforms at five different offsets: 0.1, 1.0, 2.0, 3.0, and 4.0 m. We choose $\sigma = 0.01$ S/m and the other properties are the same as in Figure 2. The amplitude is corrected for geometrical spreading (by \sqrt{r} in 2D, where r is the propagation distance).

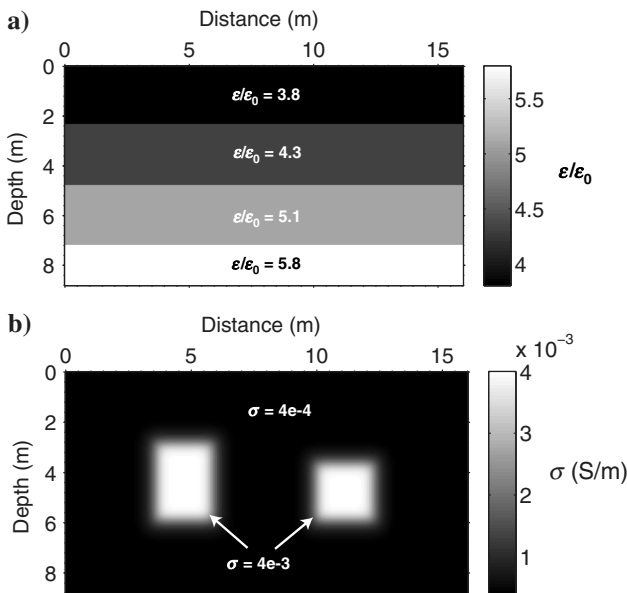


Figure 4. (a) Relative permittivity model and (b) conductivity model containing two high-conductive zones.

Three-layered model

The first test model consists of three layers. The relative dielectric permittivity model is shown in Figure 4a. There are two high conductivity zones in Figure 4b. The model is discretized with a 401×221 grid and the grid spacing is 0.04 m. We deploy 399 receivers at a depth of 0.2 m and 98 sources at 0.28 m depth, with a horizontal spacing of 0.16 m. We implement a Ricker wavelet with central frequency of $f_0 = 300$ MHz as J_x and J_z sources. The time step is 0.04 ns and the time iterations are 4000. We generate the common-shot gathers (CSG) of the H_y component by solving the TM equation (Figure 5a). Then, we extract zero-offset data from all the CSG data (Figure 5b). Due to the high conductivity in the subsurface, two shadow zones are observed in the zero-offset data, which can also be seen in the migrated image.

The image is produced by reversing time extrapolation of the zero-offset data by solving the TM equation with $s = -1$ that implies attenuation compensation. We apply the imaging condition at zero time $t = 0$; i.e., the wavefields focus at the reflectors. The attenuation compensation is stabilized by applying a frequency-wave-number Tukey low-pass filter with 600 MHz and a taper of 0.2. The cutoff frequency 600 MHz is chosen as the highest frequency for the filtered signal. Figure 6a shows the image by extrapolating zero-offset data without considering the conductivity (lossless equation), whereas Figure 6b shows the compensated imaging by extrapolating zero-offset data by considering the conductivity. The shadow

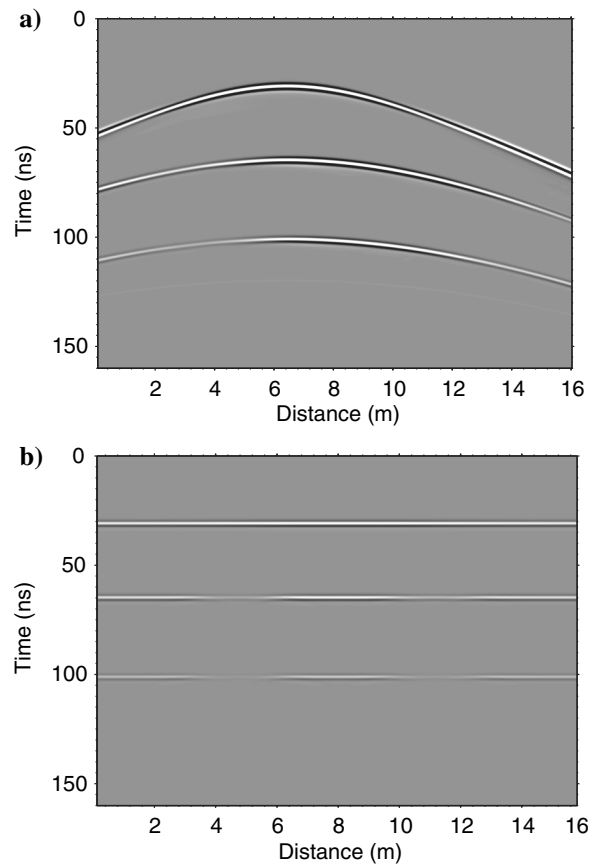


Figure 5. Synthetic radargrams of (a) the magnetic field H_y (CSG), and (b) zero-offset data extracted from all the CSGs.

zones in Figure 6a are recovered with improved illumination, and the amplitude is balanced between the highly conducting areas and the weakly conducting areas. In the shallow part, the first reflector is well imaged with both methods because low conductivity has less influence on the wave amplitude.

Figure 7 compares seismic traces at a 5 m horizontal distance, corresponding to the migrated images shown in Figure 6, with a reference image. The red line refers to the reference trace corresponding to the lossless case. The green line refers to the trace in Figure 6a using the conventional lossless imaging method, failing to recover the amplitudes and correct the dispersion effects. These differences could provide the basis of FWI of EM attenuation. The dashed black line corresponds to the trace in Figure 6b using the proposed algorithm with attenuation compensation. Compared with the reference trace (red), amplitude and phase of wavefield were recovered. Figure 7b and 7c shows details of the upper and lower events, respectively.

The spatial frequency content of all three traces is shown in Figure 8. We can see that the trace corresponding to the conventional migration lacks high wavenumbers (green curve). By compensation, high wavenumbers are almost fully recovered (black curve). Therefore, we conclude that the compensated image exhibits higher resolution than that without compensation.

Roadbed with cavity

In the second example, we consider an engineering application. The model represents an old concrete road overlying a cavity (Figure 9). Some of the material properties are taken from Lau et al.

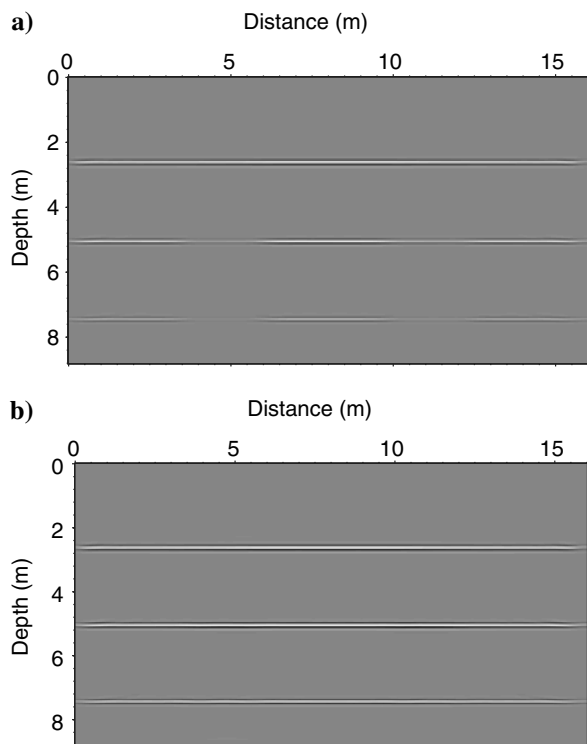


Figure 6. Migrated images. (a) Conventional (lossless) imaging; (b) the proposed imaging algorithm with attenuation compensation. Images are displayed in the same scale.

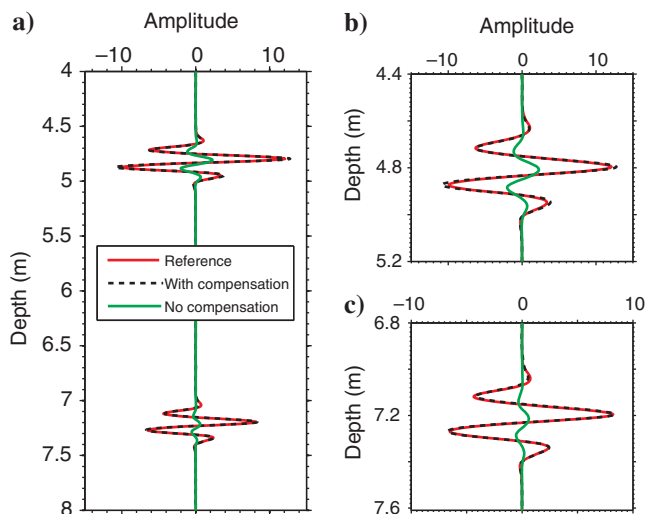


Figure 7. (a) Comparisons of traces (at 5 m) of two migrated images in Figure 6 with the reference trace (red line) computed by migration of nonattenuated GPR data. The details can be seen in panels (b and c). The dashed black line refers to the trace in Figure 6b using the proposed algorithm. The green line refers to the trace in Figure 6a using the conventional imaging.

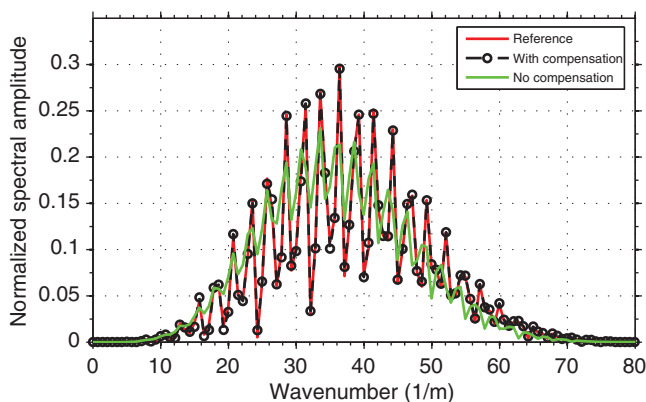


Figure 8. Wavenumber content of three traces in Figure 7.

Table 1. Relative permittivity and electrical conductivity values of the road subsurface model in Figure 9.

| Materials | Relative permittivity (ϵ/ϵ_0) | Conductivity (S/m) |
|--------------------|---|--------------------|
| Asphaltic concrete | 3.8 | 0.006 |
| Portland concrete | 5.3 | 0.009 |
| Asphalt | 5.1 | 0.0006 |
| Air | 1 | 0 |
| Rainwater | 4.3 ⁴ | 0.003 |
| Limerock | 5.8 | 0.009 |

⁴High-frequency permittivity (see equation 4 in Carcione, 1996b).

(1992) who conducted the field experiment (also see Carcione, 1996b). The dielectric permittivity and conductivity properties are given in Table 1. The cavity is filled with: case 1: air, $\epsilon = \epsilon_0$, $\sigma = 0$, and case 2: rainwater, $\epsilon = 4.3 \epsilon_0$, $\sigma = 0.003 \text{ S/m}$. Note that, in the shallow zone ($z < 0.8 \text{ m}$), the high conductivity attenuates the reflections from the cavity and other interfaces.

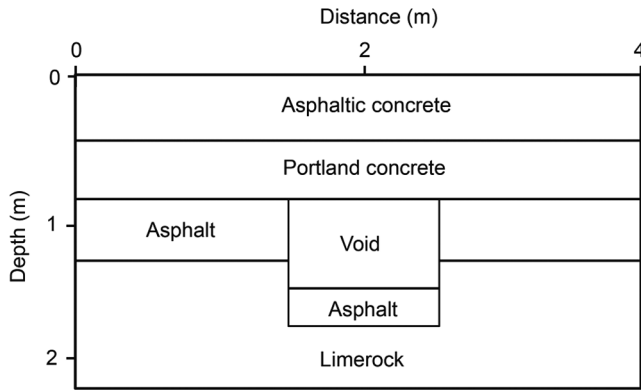


Figure 9. The geometry of the road subsurface model containing a cavity. The cavity is filled by either air (case 1) or rainwater (case 2). Electrical properties are given in Table 1.

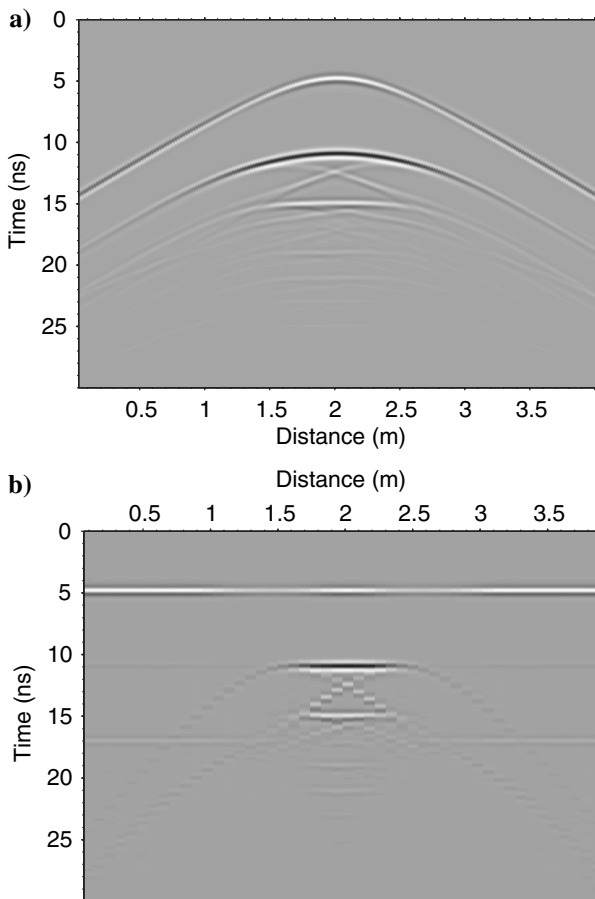


Figure 10. (a) Magnetic field radargram and (b) its corresponding zero-offset data for case 1.

The field is initiated by an electric current source. The source function is a Ricker wavelet with a central frequency of 1 GHz, and is propagated with a time step of 0.02 ns. The numerical mesh has 201×111 grid points, with a uniform grid spacing of 2 cm. We have 48 sources and 199 receivers distributed along the surface with a depth of 0.2 m.

Case 1 is the air-filled cavity. Figure 10a represents the H_y -component radargram muting the direct wave. The shot location is at the horizontal distance of 2.02 m. The first and second reflection hyperbolae correspond to the bottom of the asphaltic and Portland concrete layers, respectively. The hyperbola corresponding to the base of the asphalt layer interferes with the response generated by the bottom of the cavity (at approximately 12 ns), a response that has longer wavelength and shorter traveltimes. Similar to the first example, we also extract zero-offset data (see Figure 10b) from the CSG magnetic data.

Figure 11a shows the image by extrapolating the zero-offset data without considering conductivity (lossless equation). The first layer is well-imaged and the top of the cavity is also imaged. The rings near the reflectors are multiple reflections from the reverse time extrapolation. The image of the bottom of Portland concrete is very weak. Figure 11b shows the compensated imaging by extrapolating zero-offset data by considering the conductivity. Overall, the amplitude is recovered and the reflectors are more clearly imaged, e.g., the first reflector, the base of Portland concrete, and the asphalt layers. Image artifacts are also amplified during the attenuation compensation. The attenuation compensation is stabilized by applying a frequency-wavenumber filter with 2 GHz and a taper of 0.2, so as to avoid amplifying high-frequency noises.

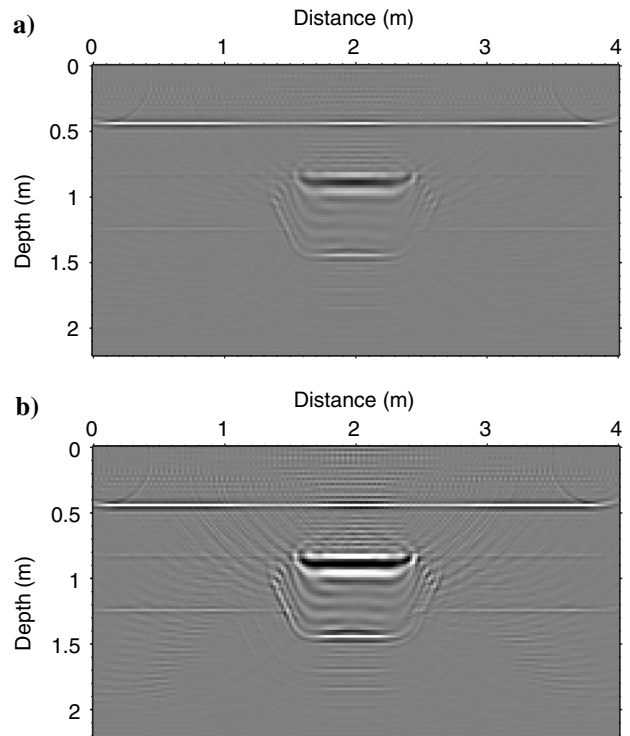


Figure 11. Migrated images of case 1. (a) Conventional imaging; (b) the proposed imaging algorithm with attenuation compensation. Images are displayed in the same scale.

For case 2 (void filled with rainwater), Figure 12 displays the H_y -component radargram and zero-offset data, respectively. Rain-water has a relatively high conductivity such that the base of the cavity is not well imaged in Figure 13a. By applying attenuation compensation, Figure 13b shows that the amplitude of the reflectors are recovered, especially the base of the void.

High conductivity water-filled layer model

The third example considers a high conductivity water-filled layer model; generally, strong radar attenuation in the water-filled reservoir prevents from reflecting at the base. The dielectric permittivity and conductivity models are shown in Figure 14. The magnetic permeability is $\mu = 4\mu_0$. The second layer has high conductivity, especially the left corner (the lowest quality factor Q is approximately 23), which dramatically attenuates reflections from the base reflector in the left side. As can be seen, this high-attenuation area prevents the imaging of the bedrock interface.

The grid size is 1001×399 and the cell spacing is 0.04 m. We use 999 receivers on the surface at a depth of 0.2 m to record the radargram and the sampling rate is 0.04 ns. The total recording length is 180 ns. For simplicity, we generate zero-offset H_y -component data using the exploding reflector modeling method. Absorbing boundary conditions are applied in all the simulations.

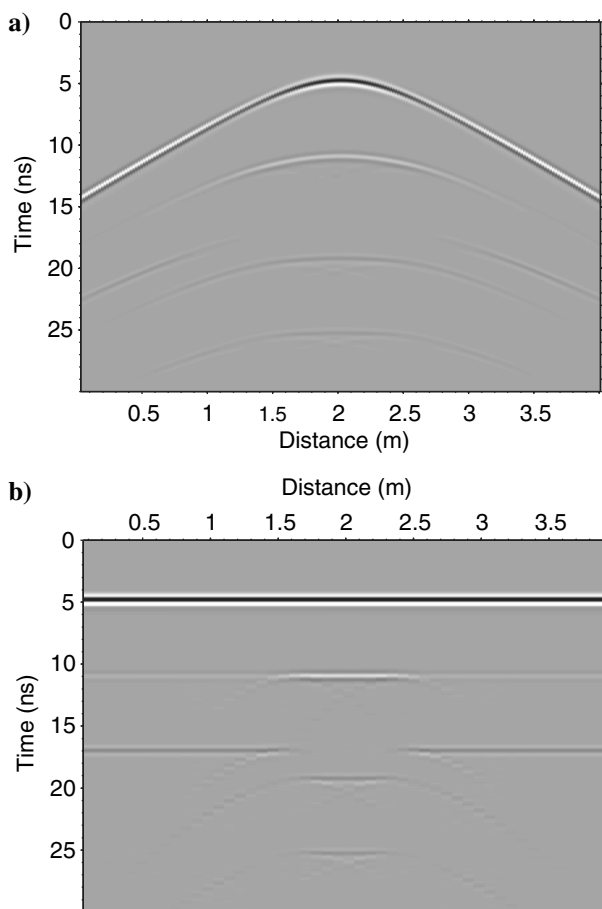


Figure 12. (a) Magnetic field radargram and (b) its corresponding zero-offset data for case 2.

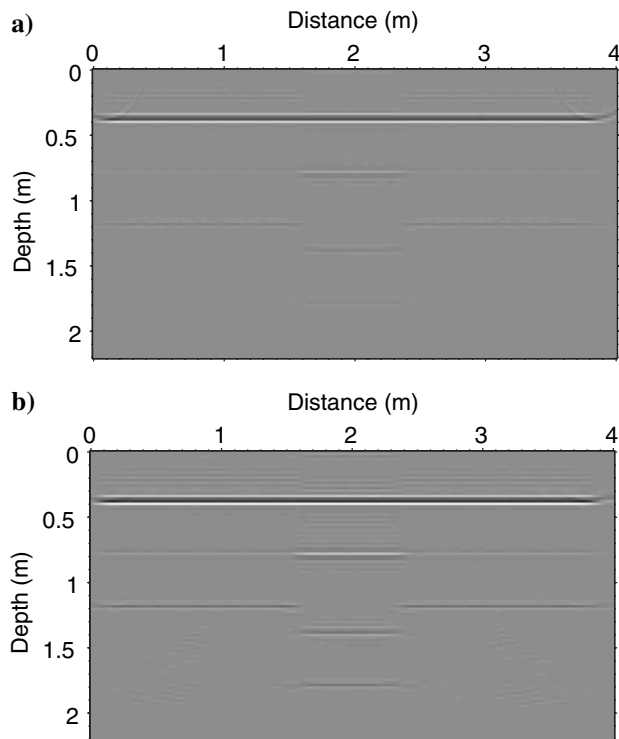


Figure 13. Migrated images of case 2. (a) Conventional imaging; (b) the proposed imaging algorithm with attenuation compensation. Images are displayed in the same scale.

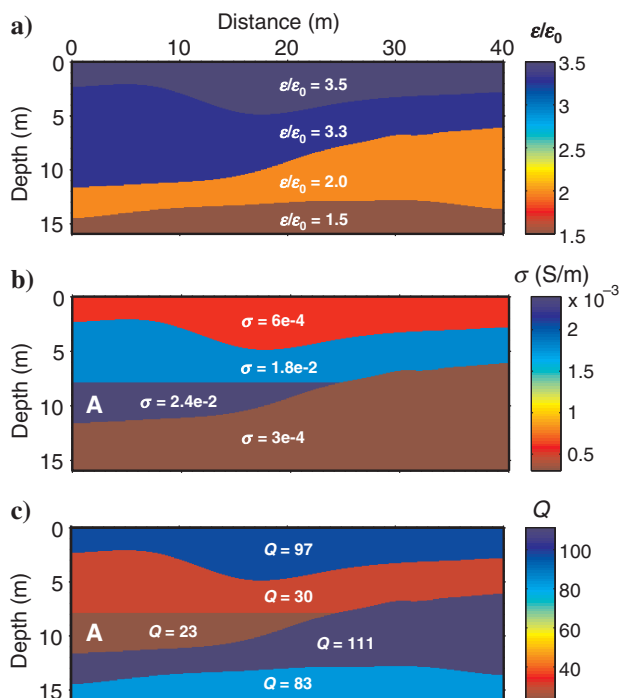


Figure 14. Relative permittivity, conductivity, and Q models of the glacier lake. Zone A exhibits high conductivity and low Q (strong attenuation).

Figure 15a shows the zero-offset data, and Figure 16a shows the imaging with the lossless equation, where dim reflectors caused by the high conductivity (attenuation) in the second layer can be observed. The bottom of the second and third layers disappear in the left side, while exhibit a weak energy in the right side. By applying attenuation compensation, the second and third reflectors are significantly enhanced as shown in Figure 16b. This image amplitude is balanced when the left shadow zone is illuminated. The attenuation compensation is stabilized by applying a frequency-wavenumber filter with 800 MHz and a taper of 0.2. The above experiment assumes that the conductivity is known from data analysis or attenuation tomography. If the conductivity is uncertain, e.g., underestimated as half the true conductivity of the second layer, we found that the image still improves (see Figure 16c). This means that attenuation compensation with an uncertain conductivity still improves the illumination of the interfaces compared with the images with zero conductivity. This new migration algorithm may be very useful for detecting the interface in such a high-attenuation model.

To test the tolerance of our migration algorithm to incoherent noise, we contaminate the zero-offset data with Gaussian random noise. Two noisy data have the signal-to-noise ratio – $S/N = 20$ dB in Figure 15b and $S/N = 10$ dB in Figure 15c. At the right side of Figure 15b and 15c, we show comparisons of traces (black) at the horizontal distance of 20 m to that of Figure 15a (gray). We repeat the migration process. Figure 17a and 17b shows the final images.

Although it is slightly contaminated by random noise, the bottom reflectors are enhanced and easily identified.

Incorporating the attenuation compensation into the migration algorithm may cause the numerical instability problem. We point out that this problem is partially solved by filtering the higher wavenumbers during the extrapolation. However, the filter may not guarantee the stability of attenuation compensation. Two factors, Q and skin depth are critical. When Q is high and thus the skin depth is larger, attenuation compensation tends to be stable. When Q is small and the skin depth is small, wave propagation with attenuation compensation may be unstable. As observed by Sena et al. (2006), attenuation compensation may be only useful for low-loss (low conductivity), i.e., media with conductive zones whose thicknesses are comparable with their characteristic skin depths computed at the dominant frequency of the radar signal.

SH-WAVE EXAMPLE

The last example illustrates SH-wave imaging based on the methodology presented above. Using the analogy between SH-wave equation and TM Maxwell equation (see equation 2), we assign the corresponding parameters G and η . Following Carcione and Cavallini (1995a), the quality factor of SH-wave is $Q_{SH} = \omega\eta/G$. The velocity and Q -factor models are shown in Figure 18a and 18b, respectively, where Q_{SH} is defined at the reference fre-

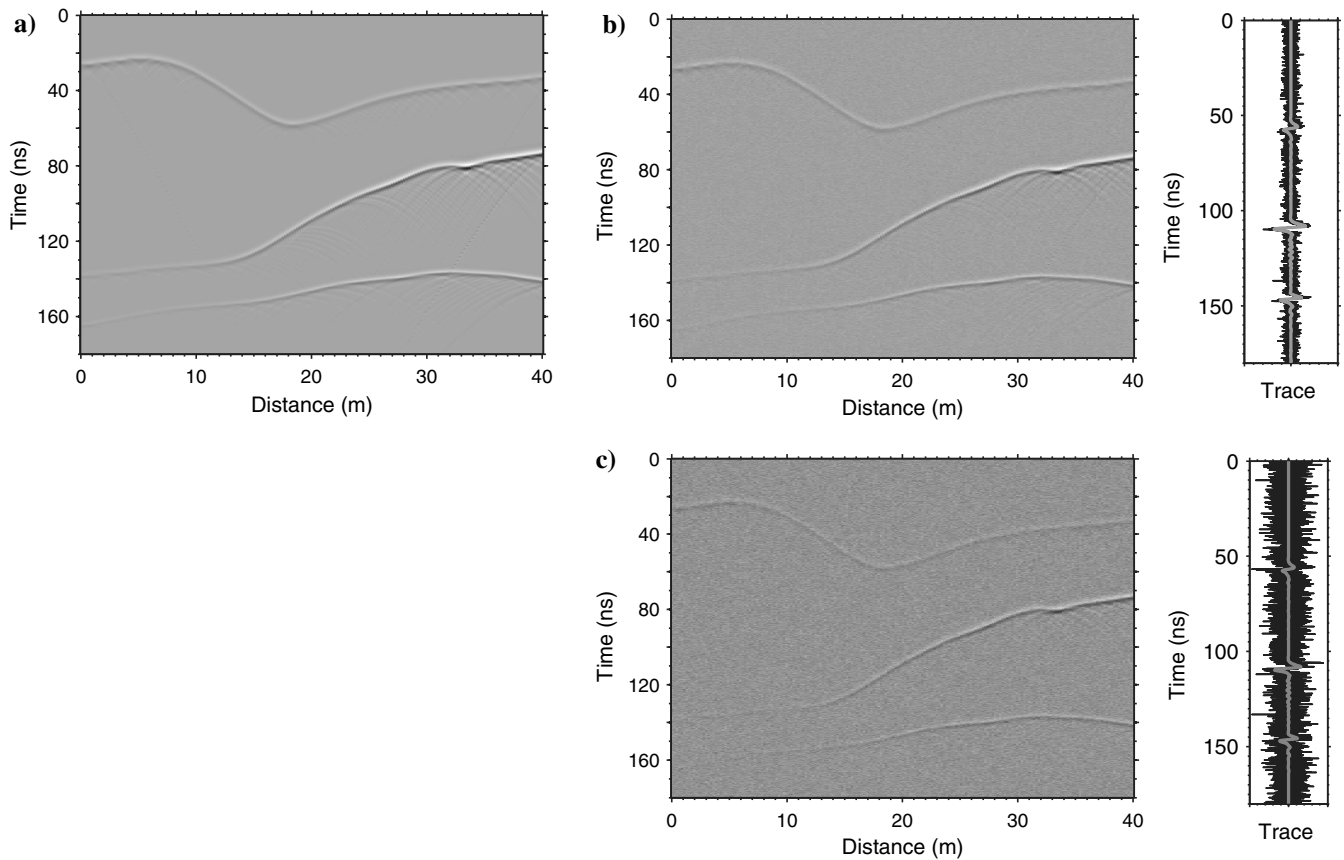


Figure 15. (a) Zero-offset magnetic field radargram computed with the exploding reflector method. (b) Noisy zero-offset radargram ($S/N = 20$ dB). (c) Noisy zero-offset radargram ($S/N = 10$ dB). The side of noisy data panels (b and c) shows comparisons of radar traces at the horizontal distance of 20 m between (a) noise-free data in gray and noisy data in black.

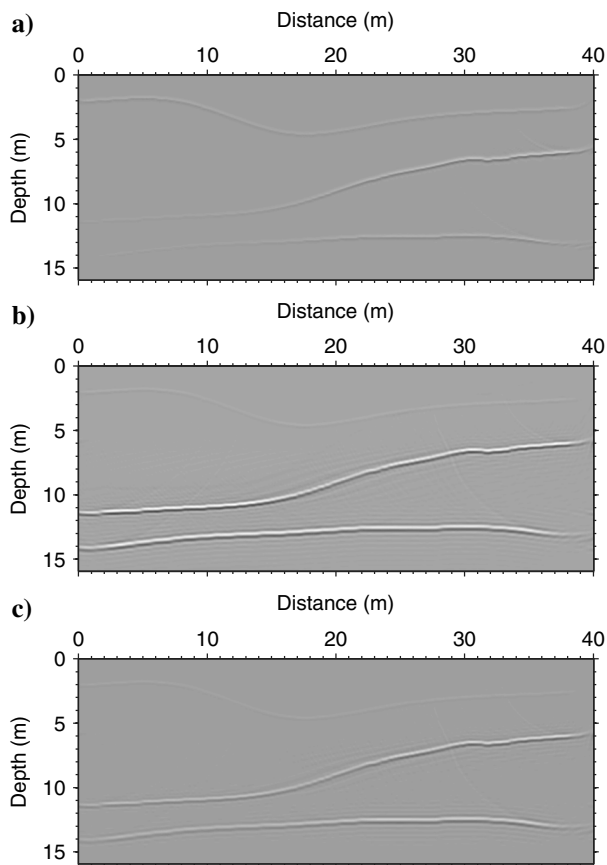


Figure 16. Migrated images by (a) conventional imaging algorithm; (b) the proposed attenuation compensated imaging algorithm with the true conductivity model; and (c) the proposed imaging algorithm with attenuation compensation but using half the true conductivity of zone A in Figure 14. All images are displayed in the same scale.

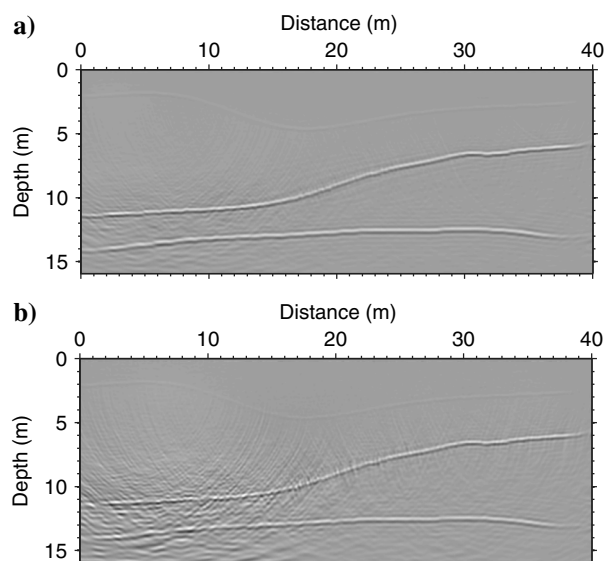


Figure 17. Migrated images computed by the proposed imaging algorithm with attenuation compensation but using noisy data (a) S/N = 20 dB and (b) S/N = 10 dB, which are shown in Figure 15. The images are displayed in the same scale as Figure 16.

quency of 30 Hz. The Q2 layer has strong attenuation, which affects the reflections from the base of the V1 and V2 layers. The cell spacing is 5 m. We locate 598 receivers at a depth of 25 m to record the seismogram. The time step is 0.5 ms and the total time step is 4500. We use a Ricker source wavelet with a central frequency of 30 Hz. A CSG (100th shot at the horizontal distance of 1.5 km) is shown in Figure 18c, where the reflection from the base of the V1 layer is relatively weaker in the left side than in the right side. Very weak reflections at 1.5 s from the base of the V2 layer are also observed.

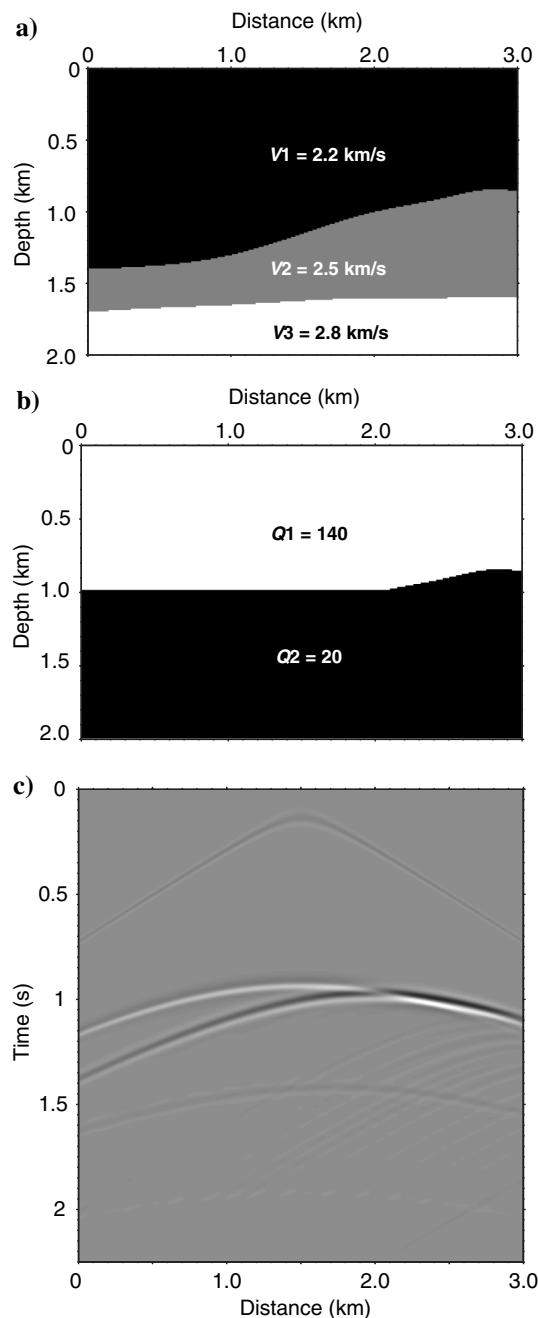


Figure 18. (a) SH-wave velocity and (b) Q model defined at the central frequency of 30 Hz. (c) A typical CSG (100th shot at the horizontal distance of 1.5 km).

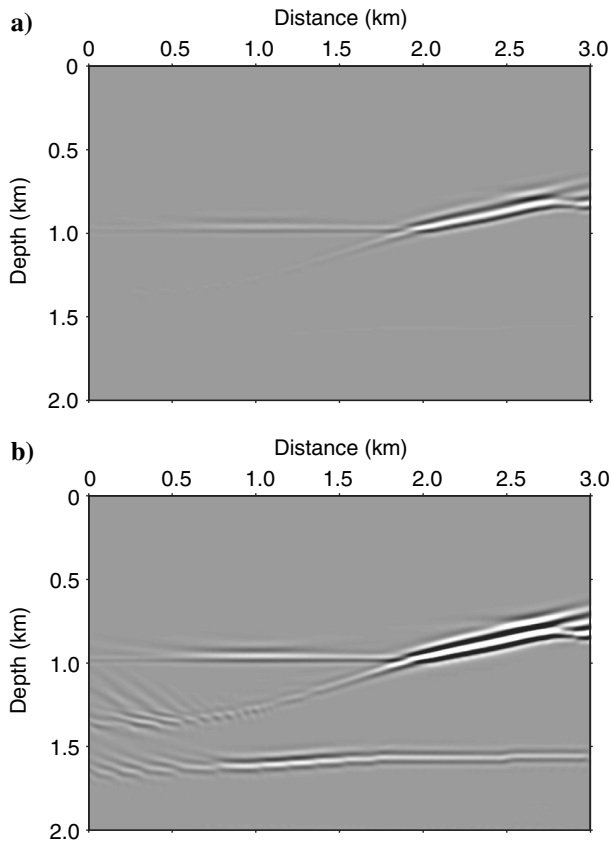


Figure 19. Migrated images by (a) conventional imaging without attenuation compensation, and (b) the proposed attenuation compensated imaging algorithm. Two images are displayed in the same scale.

Note that the top reflection is caused by the contrast between the Q1 and Q2 layers.

The imaging procedure is different from the above GPR examples. Instead of poststack (zero-offset) RTM, we use prestack RTM; i.e., we apply attenuation compensation for forward propagated source-wavefield and backward propagated receiver-wavefield. The corresponding imaging condition is equation 9. By applying the imaging approach, the resultant images are shown in Figure 19. Without attenuation compensation, the image only preserves the top reflectors (Figure 19a). Interestingly, the left side of V1 disappears, and the right side is preserved. With attenuation compensation, all reflectors appear. The left side of V1 is enhanced, and the base of V2 is clearly illuminated. Some migration artifacts are seen in the left corner, partially because of limited aperture and the nature of the finite-difference grid model (see Figure 18a).

CONCLUSION

We propose a RTM algorithm for GPR data to obtain optimal focusing (imaging) of objects and interfaces, taking into account the dispersion and attenuation effects. The back-propagation equations are obtained from the TM Maxwell equations, where the time variable has a negative sign. This compensates for the loss signal energy during the propagation, recovering the amplitudes, while it keeps the dispersion properties of Maxwell equations. This imaging

algorithm, similarly to seismic RTM, can easily be implemented in the 3D case.

The applications illustrate the feasibility of the proposed migration algorithm in the presence of high attenuation. With these examples, we are optimistic that attenuation compensation is very useful for imaging shadow zones due to high attenuation (high conductivity). Moreover, the method has applications in seismic exploration with S-waves because by virtue of the acoustic-EM analogy, the equations also describe SH-wave propagation with attenuation.

ACKNOWLEDGMENTS

The first author was supported by the Jackson Postdoctoral Fellowship at the University of Texas at Austin and the startup funding from Department of Geosciences and Institute of Natural Gas Research at the Pennsylvania State University.

REFERENCES

- Baysal, E., D. D. Kosloff, and J. W. C. Sherwood, 1983, Reverse time migration: *Geophysics*, **48**, 1514–1524, doi: [10.1190/1.1441434](https://doi.org/10.1190/1.1441434).
- Blanch, J. O., and W. W. Symes, 1995, Efficient iterative viscoacoustic linearized inversion: 65th Annual International Meeting, SEG, Expanded Abstracts, 627–630.
- Bradford, J. H., 2006, Applying reflection tomography in the postmigration domain to multifold ground-penetrating radar data: *Geophysics*, **71**, no. 1, K1–K8, doi: [10.1190/1.2159051](https://doi.org/10.1190/1.2159051).
- Bradford, J. H., 2015, Reverse-time prestack depth migration of GPR data from topography for amplitude reconstruction in complex environments: *Journal of Earth Science*, **26**, 791–798, doi: [10.1007/s12583-015-0596-x](https://doi.org/10.1007/s12583-015-0596-x).
- Busch, S., J. van der Kruk, J. Bikowski, and H. Vereecken, 2012, Quantitative conductivity and permittivity estimation using full-waveform inversion of on-ground GPR data: *Geophysics*, **77**, no. 6, H79–H91, doi: [10.1190/geo2012-0045.1](https://doi.org/10.1190/geo2012-0045.1).
- Carcione, J. M., 1996a, Ground penetrating radar: Wave theory and numerical simulation in conducting anisotropic media: *Geophysics*, **61**, 1664–1677, doi: [10.1190/1.1444085](https://doi.org/10.1190/1.1444085).
- Carcione, J. M., 1996b, Ground-radar numerical modeling applied to engineering problems: *European Journal of Environmental and Engineering Geophysics*, **1**, 65–81.
- Carcione, J. M., 2014, Wave fields in real media: Wave propagation in anisotropic, anelastic, porous and electromagnetic media: *Handbook of geophysical exploration*: Elsevier.
- Carcione, J. M., and F. Cavallini, 1995a, On the acoustic-electromagnetic analogy: *Wave Motion*, **21**, 149–162, doi: [10.1016/0165-2125\(94\)00047-9](https://doi.org/10.1016/0165-2125(94)00047-9).
- Carcione, J. M., and F. Cavallini, 1995b, The generalized SH wave equation: *Geophysics*, **60**, 549–555, doi: [10.1190/1.1443792](https://doi.org/10.1190/1.1443792).
- Carcione, J. M., G. Lenzi, and S. Valle, 1999, GPR modeling by the Fourier method: Improvement of the algorithm: *Geophysical Prospecting*, **47**, 1015–1029, doi: [10.1046/j.1365-2478.1999.00151.x](https://doi.org/10.1046/j.1365-2478.1999.00151.x).
- Carcione, J. M., L. Piñero Feliciangeli, and M. Zamparo, 2002, The exploding-reflector concept for ground penetrating radar modeling: *Annals of Geophysics*, **45**, 473–478, doi: [10.4401/ag-3526](https://doi.org/10.4401/ag-3526).
- Claerbout, J. F., 1985, *Imaging the earth's interior*: Blackwell Scientific Publications.
- Dai, N., and G. F. West, 1994, Inverse Q migration: 64th Annual International Meeting, SEG, Expanded Abstracts, 1418–1421, doi: [10.1190/1.1822799](https://doi.org/10.1190/1.1822799).
- Di, Q., and M. Wang, 2004, Migration of ground-penetrating radar data with a finite-element method that considers attenuation and dispersion: *Geophysics*, **69**, 472–477, doi: [10.1190/1.1707067](https://doi.org/10.1190/1.1707067).
- Dutta, G., and G. T. Schuster, 2014, Attenuation compensation for least-squares reverse time migration using the viscoacoustic-wave equation: *Geophysics*, **79**, no. 6, S251–S262, doi: [10.1190/geo2013-0414.1](https://doi.org/10.1190/geo2013-0414.1).
- Fischer, E., G. A. McMechan, A. P. Annan, and S. W. Cosway, 1992, Examples of reverse-time migration of single-channel, ground-penetrating radar profiles: *Geophysics*, **57**, 577–586, doi: [10.1190/1.1443271](https://doi.org/10.1190/1.1443271).
- Hinz, E. A., and J. H. Bradford, 2010, Ground-penetrating-radar reflection attenuation tomography with an adaptive mesh: *Geophysics*, **75**, no. 4, WA251–WA261, doi: [10.1190/1.3467874](https://doi.org/10.1190/1.3467874).
- Kjartansson, E., 1979, Constant Q-wave propagation and attenuation: *Journal of Geophysical Research*, **84**, 4737–4748, doi: [10.1029/JB084iB09p04737](https://doi.org/10.1029/JB084iB09p04737).
- Lau, C. L., T. Scullion, and P. Chan, 1992, Using ground penetrating radar technology for pavement evaluations in Texas, USA: 4th International

- Conference on Ground Penetrating Radar, Finland Geological Survey, Special Paper 16, 277–283.
- Lavoué, F., R. Brossier, L. Métivier, S. Garambois, and J. Virieux, 2014, Two-dimensional permittivity and conductivity imaging by full waveform inversion of multioffset GPR data: A frequency-domain quasi-Newton approach: *Geophysical Journal International*, **197**, 248–268, doi: [10.1093/gji/ggt528](https://doi.org/10.1093/gji/ggt528).
- Liu, L., J. W. Lane, and Y. Quan, 1998, Radar attenuation tomography using the centroid frequency downshift method: *Journal of Applied Geophysics*, **40**, 105–116, doi: [10.1016/S0926-9851\(98\)00024-X](https://doi.org/10.1016/S0926-9851(98)00024-X).
- McMechan, G. A., 1983, Migration by extrapolation of time-dependent boundary values: *Geophysical Prospecting*, **31**, 413–420, doi: [10.1111/j.1365-2478.1983.tb01060.x](https://doi.org/10.1111/j.1365-2478.1983.tb01060.x).
- Miller, R. D., J. H. Bradford, K. Holliger, and R. B. Latimer, 2010, Advances in near-surface seismology and ground-penetrating radar: SEG.
- Owen, T. E., 1995, Editors page, Special issue on ground penetrating radar: *Journal of Applied Geophysics*, **33**, 5–6, doi: [10.1016/0926-9851\(95\)90024-1](https://doi.org/10.1016/0926-9851(95)90024-1).
- Özdemir, C., F. Demirci, E. Yiğit, and B. Yılmaz, 2014, A review on migration methods in B-Scan ground penetrating radar imaging: *Mathematical Problems in Engineering*, **2014**, 280738, doi: [10.1155/2014/280738](https://doi.org/10.1155/2014/280738).
- Pestana, R. C., and M. A. B. Botelho, 1997, Migração de dados de radar (GPR) com correção topográfica simultânea: *Revista Brasileira de Geofísica*, **15**, 3–10, doi: [10.1590/S0102-261X1997000100001](https://doi.org/10.1590/S0102-261X1997000100001).
- Sena, A. R., P. L. Stoffa, and M. K. Sen, 2006, Split-step Fourier migration of GPR data in lossy media: *Geophysics*, **71**, no. 4, K77–K91, doi: [10.1190/1.2217157](https://doi.org/10.1190/1.2217157).
- Slob, E., M. Sato, and G. Olhoeft, 2010, Surface and borehole ground-penetrating-radar developments: *Geophysics*, **75**, no. 5, 75A103–75A120, doi: [10.1190/1.3480619](https://doi.org/10.1190/1.3480619).
- Sun, J., S. Fomel, and T. Zhu, 2015, Preconditioning least-squares RTM in viscoacoustic media by Q-compensated RTM: 80th Annual International Meeting, SEG, Expanded Abstracts, 3959–3965.
- Yu, Y., R. S. Liu, and M. M. Deal, 2002, Compensation for the effects of shallow gas attenuation with viscoacoustic wave equation migration: 72nd Annual International Meeting, SEG, Expanded Abstracts, 2062–2065, doi: [10.1190/1.1817107](https://doi.org/10.1190/1.1817107).
- Yuan, X., D. Borup, J. Wiskin, M. Berggren, and S. A. Johnson, 1999, Simulation of acoustic wave propagation in dispersive media with relaxation losses by using FDTD method with PML absorbing boundary condition: *IEEE Transactions on Ultrasonics, Ferroelectrics, and Frequency Control*, **46**, 1423.
- Zhang, Y., P. Zhang, and H. Zhang, 2010, Compensating for visco-acoustic effects in reverse-time migration: 80th Annual International Meeting, SEG, Expanded Abstracts, 3160–3164.
- Zhdanov, M., 2009, *Geophysical electromagnetic theory and methods: Methods in geochemistry and geophysics*: Elsevier.
- Zhdanov, M., and M. Frenkel, 1983, The solution of the inverse problems on the basis of the analytical continuation of the transient electromagnetic field in the reverse time: *Journal of Geomagnetism and Geoelectricity*, **35**, 747–765, doi: [10.5636/jgg.35.747](https://doi.org/10.5636/jgg.35.747).
- Zhou, H., M. Sato, and H. Liu, 2005, Migration velocity analysis and prestack migration of common-transmitter ground-penetrating radar data: *IEEE Transactions on Geoscience and Remote Sensing*, **43**, 86–91, doi: [10.1109/TGRS.2004.839920](https://doi.org/10.1109/TGRS.2004.839920).
- Zhu, T., 2014, Time-reverse modeling of acoustic wave propagation in attenuating media: *Geophysical Journal International*, **197**, 483–494, doi: [10.1093/gji/ggt519](https://doi.org/10.1093/gji/ggt519).
- Zhu, T., 2015, Implementation aspects of attenuation compensation in reverse-time migration: *Geophysical Prospecting*, doi: [10.1111/1365-2478.12301](https://doi.org/10.1111/1365-2478.12301).
- Zhu, T., and J. M. Harris, 2014, Modeling acoustic wave propagation in heterogeneous attenuating media using decoupled fractional Laplacians: *Geophysics*, **79**, no. 3, S165–S174, doi: [10.1190/geo2013-0245.1](https://doi.org/10.1190/geo2013-0245.1).
- Zhu, T., and J. M. Harris, 2015, Improved seismic image by Q-compensated reverse time migration: Application to crosswell field data, west Texas: *Geophysics*, **80**, no. 2, B61–B67, doi: [10.1190/geo2014-0463.1](https://doi.org/10.1190/geo2014-0463.1).
- Zhu, T., J. M. Harris, and B. Biondi, 2014, Q-compensated reverse-time migration: *Geophysics*, **79**, no. 3, S77–S87, doi: [10.1190/geo2013-0344.1](https://doi.org/10.1190/geo2013-0344.1).